

Deep Learning-Based Position Detection for Hydraulic Cylinders Using Scattering Parameters

Chen Xin^{a,b}, Thomas Motz^b, Wolfgang Fuhl^a, Andreas Hartel^b, Enkelejda Kasneci^{c,*}

^aEberhard Karls University of Tübingen, Sand 14, Tübingen, 72076, Germany

^bLiebherr-Electronics and Drives GmbH, Peter-Dornier-Straße 11, Lindau (Bodensee), 88131, Germany

^cTechnical University of Munich, Arcisstraße 21, München, 80333, Germany

Abstract

Position detection of hydraulic cylinder pistons is crucial for numerous industrial automation applications. A typical traditional method is to excite electromagnetic waves in the cylinder structure and analytically solve the piston position based on the scattering parameters measured by a sensor. The core of this approach is a physical model that outlines the relationship between the measured scattering parameters and the targeted piston position. However, this physical model has shortcomings in accuracy and adaptability, especially in extreme conditions. To address these limitations, we propose machine learning and deep learning-based methods to learn the relationship directly in a data-driven manner. As a result, all deep learning models in this paper consistently outperform the physical one by a large margin. We further deliberate on the choice of models based on domain knowledge and provide in-depth analyses combining model performance with real-world physical characteristics. Specifically, we use Convolutional Neural Network (CNN) to discover local interactions of input among adjacent frequencies, apply Complex-Valued Neural Network (CVNN) to exploit the complex-valued nature of electromagnetic scattering parameters, and introduce a novel technique named Frequency Encoding to add weighted frequency information to the model input. The combination of these techniques results in our best-performing model, a complex-valued CNN with Frequency Encoding, which exhibits substantial improvement in accuracy with an error reduction of 1/12 compared to the traditional physical model.

Keywords: Deep learning, convolutional neural network, complex-valued neural network, frequency encoding, position detection, scattering parameter

1. Introduction

The ubiquitous aim for automation in industrial processes demands accurate control of their components. To better control the working behavior of a hydraulic cylinder, one of the most widely used components in industrial automation applications, we need to know the precise position of its piston. LiView (Figure 1) is a sensor that can emit microwave signals and intercept their reflections inside a hydraulic cylinder to detect the piston position.

One can model the physical relationship between the microwave signals and the current piston position by

interpreting the cylinder as a linear electrical network to compute the exact value of the current piston position. This network is coupled to ports that are excited by the incident and reflected voltage waves that reflect the interaction of the electromagnetic waves and the cylinder (White, 2004). The whole network can then be formalized by a linear equation, where its coefficients, the scattering parameters, convey the excitation of the ports and detailed model assumptions of the network. After measuring these scattering parameters, we can use the mathematical expression of the network in reverse to deduce the piston position. However, due to the high demand for positional accuracy, the calculation of piston position based on the physical model, the linear electrical network based on the scattering matrix, is problematic. One of the arguments is that the model performance deteriorates severely in harsh environments and challenging use cases because extreme

*Corresponding author

Email addresses: chen.xin@uni-tuebingen.de (Chen Xin), thomas.motz@liebherr.com (Thomas Motz), wolfgang.fuhl@uni-tuebingen.de (Wolfgang Fuhl), andreas.hartel@liebherr.com (Andreas Hartel), enkelejda.kasneci@tum.de (Enkelejda Kasneci)

conditions invalidate the physical model. Additionally, the sensor should function properly and guarantee high accuracy in a large variety of temperatures, mechanical stress, moisture, and dust, which is precisely the weakness of the approach based on the physical model, given its poor consistency and robustness. On the contrary, these requirements make the learning-based methods seem more promising.

Machine learning is the process of using adaptive models to analyze and understand patterns in data, and make predictions without explicit programming. A typical workflow is to hand-design good features from raw data, and then the machine learning models are trained in to map the generated features to the corresponding target. However, the feature extraction from scattering parameters is a nontrivial task that requires in-depth domain expertise, The quality of the features directly affects the accuracy. We confirm this through experiments, where we apply classical machine learning models directly to the raw data and are not able to achieve satisfactory results. Due to the complexity of the environment inside the cylinder, we do not force meticulous engineering on handcrafted features but pin our hopes on deep learning instead.

Deep learning, or Artificial Neural Network (ANN), as an important branch of machine learning, provides a way to avoid the necessity for handcrafted features. It allows models composed of multiple processing layers to learn data representations with multiple levels of abstraction automatically. Two quintessential examples of ANNs are Multilayer Perceptron (MLP) and Convolutional Neural Network (CNN), which are multilayer stacks of fully connected and convolutional layers, respectively. In this paper, we explore the feasibility of MLPs and CNNs for piston position detection based on scattering parameters. In all our experiments, deep learning-based models consistently outperform both the traditional physical model and classical machine learning models by a large margin. We also investigate the particular impact of general architectures and components of MLPs and CNNs for this specific task. We find that different activation functions and the application of convolution have significant effects on the model performance for our specific task. We offer explanations in the context of the characteristics of the model and the physical nature of hydraulic cylinders.

The aforementioned machine learning and deep learning models mainly focus on real-valued data. However, scattering parameters are complex numbers. One way to cope with complex numbers is to break a complex-valued vector into its real and imaginary parts to form a real-valued vector of two times the length

of the original complex-valued vector. This simple approach effortlessly translates the problem from the complex domain to the real domain but the essential statistical information, such as the correlation between the real and imaginary parts of the numbers is completely lost. On the other hand, Complex-Valued Neural Network (CVNN) with complex-valued weights, such as complex-valued MLP (Hirose, 2012; Sarroff, 2018) and complex-valued CNN (Trabelsi et al., 2018; Zhang et al., 2017), solve the problem directly in the complex domain. They are designed to have more constraints to force the model to mimic calculations in the complex domain. This way, more information about the specific application is introduced to the model, which could improve the model performance. In this paper, we show that our CVNN versions of MLP and CNN both substantially outperform their real-valued counterparts.

In addition to internalizing the information that the model should operate in the complex domain by CVNN, other information related to the input can also be introduced into the model by simply adding the information to the input itself. For example, in the original transformer model (Vaswani et al., 2017), the position information of the input words is encoded and added directly to the word embedding. Inspired by this idea, we also applied a model-agnostic technique named Frequency Encoding to add frequency information to our model input after weighting by learnable parameters. To our best knowledge, this is the first work to use frequency information of electromagnetic waves by adding a learned weighted encoding of it directly to the model input. This simple trick significantly improves the model performance by about 36% for both MLP and CNN framework.

Machine learning (Roshani et al., 2021; Akhavanhejazi et al., 2011; Barbosa et al., 2019; Rana et al., 2019; Bader et al., 2021; Hejazi et al., 2011) and deep learning (Hien and Hong, 2021; Frazier et al., 2022; Husby et al., 2019; Gupta, 2020; Travassos et al., 2020; Rana et al., 2019) have already caught the attention of previous researchers in scattering parameter related projects. Despite the notable achievements in accuracy, there are still some regretful missing aspects. We consistently find the following pattern in papers in this area: the authors take a great deal of effort to design an elaborate physical experiment but only present a standard machine learning or deep learning model without the motivation for the choice of their specific models, the comparison between different models, and their connections to the real-world physical system. In contrast, we keep the physical model unchanged and focus on designing the best deep learning models. We find that our

best deep learning model designed under the guidance of physical properties can perform 4 times better than a standard one with similar model parameters. This is strong evidence of the potential of dedicated deep learning models in the area of scattering parameter-related projects.

In this paper, we propose promising deep learning models for piston detection using scattering parameters. We elaborate on the motivations for the chosen models, compare the performance of different learning-based models, conjecture possible model improvements based on the physical system, and prove our assumptions by in-depth analyses based on the model characteristics and physical nature of the task. We hope this paper can serve as a guide for projects in the area of deep learning using scattering parameters and a reminder of the potential of dedicated deep learning models. Our major findings and contributions are as follows:

1. Deep learning-based models significantly and consistently outperform both the traditional physical model and classical machine learning models. The relative error of the most accurate model, a complex-valued CNN with Frequency Encoding (FE), is less than 1/12 of the traditional physical model.
2. Frequency Encoding dramatically improves the generalization performance of all ANN based models at a negligible cost of extra trainable parameters and without the need to change the backbone structure of the model.
3. Complex-Valued Neural Networks outperform their real-valued counterparts by a large margin, which is strong evidence that more emphasis should be placed on the complex nature of the specific task.
4. CNNs consistently beat MLPs on performance, indicating the local interactions between frequencies play an important role.
5. The performance of models with the same architecture, but different activation functions varies greatly, implying that a function choice that more closely matches the physical characteristics of the task is preferred, especially when computational resources limit the total number of parameters of the model.

The rest of the paper is organized as follows. In section 2, we summarize the achievements and our inspirations from them. Then in section 3, we show the physical characteristics by formalizing the physical model. All the machine learning (Random Forest (RF) and Gradient Boosted Decision Tree (GBDT) in section 4.1),

and deep learning models (MLP and CNN in section 4.2) including CVNN (section 4.3) are presented in section 4, together with the novel technique Frequency Encoding (section 4.4). In section 5, we introduce the dataset (section 5.1), specify the implementation details (section 5.2), evaluate the model performance in accuracy (section 5.3) and lastly discuss model complexity in terms of parameter numbers and inference speed (section 5.4). Finally, section 6 provides our conclusions.

2. Related Work

Physical Model-Based Approaches. Given the characteristics of the interior of hydraulic cylinders, electromagnetic wave is a good medium for detecting the piston position. Compared to alternatives like optical systems or cable potentiometers, a sensor based on electromagnetic waves is less exposed to external perturbations since the measurement depends solely on the cylinder's interior. There are some varieties of attempts to measure the piston position with electromagnetic signals. The difference lies in whether coupling the signal into the cylinder on the side of the piston where the rod is present (Morgan, 1994-06-28; Braun et al., 2014-01-17, 2017-04-05) or on the other side without the rod (Fend et al., 2011-06-30; Büchler et al., 2011-06-30). In the first situation, the cylinder tube and piston rod form a coaxial cavity, while the latter leads to a signal propagating in a hollow waveguide of variable length. Both variants can be modeled so that the position of the cylinder can be extracted, for example, from the analysis of resonant frequencies. The physical model we adopt for the comparison to our deep learning models is the LiView system (section 3). It belongs to the first category. A detailed description of it can be found in section 3. In short, we model the cylinder as a three-port electrical system (Equation 3) and derive equations (see Equations 6 and 8) describing the relationship between the target piston position and our sensor measurements. The equations are solvable only if we make some reasonable assumptions and fix the values of some variables by means of calibrations in advance. However, the variable assumptions could break in harsh environments and the model assumptions are not exactly accurate in extreme conditions, which leads to noisy and inaccurate position detections. Learning-based methods overcome these restrictions and allow for a generic modeling process for various environments.

Machine Learning-Based Approaches. Classical machine learning algorithms, such as Support Vector Machine (SVM), K-Nearest-Neighbor (k-NN), Decision Tree (DT) have been widely adopted in industrial

applications (Bertolini et al., 2021; Kang et al., 2020; Narciso and Martins, 2020). Machine Learning has also become a popular choice to find the relationship between the input scattering parameters and the desired target. For instance, a k-NN-based method for online monitoring of transformer winding axial displacement using scattering parameters is presented in Hejazi et al. (2011). The closeness among samples is measured in terms of Euclidean distance in the feature space consisting of the magnitude and phase of the measured scattering parameters. Researchers in the same group used the same feature space but replace k-NN with Classification And Regression Trees (CART) (Breiman et al., 1984) to detect the axial position of the winding (Akhavanhejazi et al., 2011). Both k-NN and DT were able to detect the position of the winding (displacement) with acceptable relative errors (smaller than 0.2%). But this performance could only be achieved after storing enough reference feature vectors in advance. In recent studies, classical machine learning approaches are still popular. Bader et al. (2021) investigated a cable identification method using SVM based on scattering parameters. The real and imaginary parts of the complex-valued scattering parameters and their magnitudes were used as the input of a linear SVM which achieved an accuracy close to 100%. Despite the promising results, the applications mentioned above are rooted in relatively simple systems (specifically two-port networks simulated in the lab). In this paper, we used two more sophisticated machine learning models, RF and GBDT, to handle more complicated (three-port network) and noisy real-world experiments. But without forcing meticulous feature engineering, machine learning models do not perform as well as deep learning models.

Deep Learning-Based Approaches. Deep Learning has attracted the attention of researchers working with scattering parameters due to its strong potential both in theory and in practice. Husby et al. (2019) adopted 3-hidden-layer MLP with ReLU activation to detect the thickness of duplex coatings used for corrosion protection of carbon steel substrates. They concatenated the real and imaginary components of the measured scattering parameters into a real vector with doubled dimensions as the input to the MLP. They were able to reduce the relative standard deviation to 2.5%. Hien and Hong (2021) proposed a material thickness classification with the help of a 6-hidden-layer MLP also with ReLU activation using features derived from scattering parameters. Besides real and imaginary parts of the scattering parameters as in Bader et al. (2021), they also used frequency, relative permittivity, and loss tangent directly to form the dimensions of the input fea-

ture vectors. They binned the ground truth into eight thickness classes and recorded impeccable average estimation accuracy. Similarly, In addition to MLP, CNN can also be of help. Gupta (2020) described a CNN based hand movement classification from scattering parameters. Likewise, they also fed their model with extra features calculated from recorded scattering parameters and finally achieved an accuracy of 98%. Given the above successful demonstrations, we also evaluated MLP and CNN with reasonable adaptations (section 4.2 and 5.2) to fit our task. Note that all previously mentioned models in this section are real-valued models but with complex-valued input. A common way to solve this contradiction is to concatenate a complex-valued vector's real and imaginary parts to form a double-sized real-valued vector. We adopted this way to construct our real-valued models as well, but also implemented CVNNs to handle complex-valued input directly.

Complex-Valued Neural Network (CVNN) complex numbers are often used in many real-world practical applications, such as in telecommunications, robotics, bioinformatics, image processing, sonar, radar, and speech recognition (Bassey et al., 2021). Scattering parameters are also complex numbers. To deal with them directly in the complex domain, CVNN is a good option. Yang and Bose (2005) applied CVNN for landmine detection based on scattering parameters. They trained CVNN with a single hidden layer on a highly unbalanced small dataset. This can only result in a good average true positive rate after strict outlier removal and data balancing. In a recent study, Frazier et al. (2022) investigated CVNN more thoroughly in their application for the estimation of complex reverberant wave fields using complex-valued scattering parameter as input. They tested a CVNN with complex-valued weights and a hybrid ANN which processes real and imaginary parts of the input independently and only combines these two parts at the very end of the model to generate the output. They compared these two versions of CVNN with their real-valued counterpart and found out that the CVNN with complex-valued weights achieved the best performance and outperformed the real-valued model based only on the magnitude of the scattering parameters by a large margin. Besides complex-valued MLP in the above-mentioned two projects, complex-valued CNNs also achieved promising results in other areas, such as image recognition in Trabelsi et al. (2018). Encouraged by these results, we also implemented both complex-valued MLP and complex-valued CNN for our project and show that they outperform their real-valued counterparts by a large margin.

Frequency Encoding. In the aforementioned work,

it’s common to use not only scattering parameters but also other extra useful features either deriving from scattering parameters or related to the experimental setup, such as voltage standing wave ratio in Gupta (2020) or permittivity in Hien and Hong (2021). However, these extra features, although directly related to the original input, are usually concatenated to the original input, which increases the input dimension and therefore the model size significantly. Another way to introduce additional information to the model is to add extra information to the original input. A typical example is the positional encoding for the Transformer (Vaswani et al., 2017), where sinusoidal functions encode the position of each word (of the input sentence), and the code is directly added to the input embedding. Inspired by the idea of positional encoding, we designed a novel technique called Frequency Encoding, which inserts the frequency information into the model in an additive (rather than concatenative as in previous works) way. The difference between positional encoding and our Frequency Encoding is that we do not encode the frequency in a predefined way but with learnable parameters.

Despite the notable achievements of the papers in the area of machine learning and deep learning based on scattering parameters, there are still some regretful missing parts. Firstly, the computational resource doesn’t seem to be a concern for most of the work. Considering the model deployment in an edge computing device in the future, we restrict the model parameters to 10K and provide detailed analyses of the tradeoff between model performance and model size. Secondly, previous works in this area tend to directly adopt standard deep learning models without customization based on the task at hand. The researchers focus more on the design of physical experiments but usually simply pick a standard deep learning model without the analysis of their specific models and the comparison between different models. We are often unable to find a detailed analysis of the test results, not to mention linking the model performance to practice by explaining why the model works in view of both the properties of the chosen machine learning or deep learning models and the physical characteristics of the system. In our opinion, the motivation and analyses serve as helpful guidance for similar projects in the future. Therefore, we focus on the design of the deep learning model in combination with the physical characteristics of the system. We provide in-depth analyses of the motivation for our model choices (section 4), and the evaluation of our models’ performance (section 5.3). But before all that, we will start our journey by introducing our physical model.

3. Physical Model

The physical model is based on the LiView system. LiView is a sensor that measures the current position of the piston in a hydraulic cylinder via the analysis of electrical fields that are excited within the cylinder (Braun et al., 2017-04-05). It feeds microwave signals with frequencies in a range from 300 MHz to 1.5 GHz into the cylinder and measures the signals reflected by the cylinder structure. The measured data provide signatures that allow a determination of the piston position after the read-out of them.

As shown in Figure 1a, the LiView system consists of an electronic unit positioned outside the cylinder and two probes connecting the cylinder’s interior with the electronic unit via two coaxial wires. These wires conduct a microwave signal (illustrated as arrows in Figure 1b) that is generated in the electronic unit and capacitively fed into the cylinder (Leutenegger et al., 2017-12-15). The electrical fields that propagate through the cylinder have frequencies in a range from 300 MHz to 1.5 GHz with their phases and amplitudes depending on the piston position.

In the present frequency regime, it is common to employ a formalism based on wave quantities that describe scattering on the linear electrical network that represents the investigated system (White, 2004), (Ludwig and Bretchko, 2000). Given the incident and reflected voltage wave, E_i^{inc} and E_i^{ref} , of a port i , we define two waves a_i and b_i as

$$a_i = \frac{E_i^{inc}}{\sqrt{Z_0}}, \quad (1)$$

$$b_i = \frac{E_i^{ref}}{\sqrt{Z_0}}, \quad (2)$$

where Z_0 is the transmission line’s characteristic impedance, which connects the i^{th} port. With the help of a and b waves, a linear electrical network can be characterized by a set of coupled algebraic equations describing the reflected waves from each port in terms of the incident waves at all the ports (White, 2004). The coefficients of the network are called the scattering parameters S . For a three-port electrical system as the LiView system, the network can be described in the matrix format:

$$\begin{pmatrix} b_1 \\ b_2 \\ b_3 \end{pmatrix} = \begin{bmatrix} S_{11} & S_{12} & S_{13} \\ S_{21} & S_{22} & S_{23} \\ S_{31} & S_{32} & S_{33} \end{bmatrix} \begin{pmatrix} a_1 \\ a_2 \\ a_3 \end{pmatrix}. \quad (3)$$

Figure 2 provides an abstract illustration of the three-port network which models the LiView system. It is a linear electrical network that interacts with three ports.

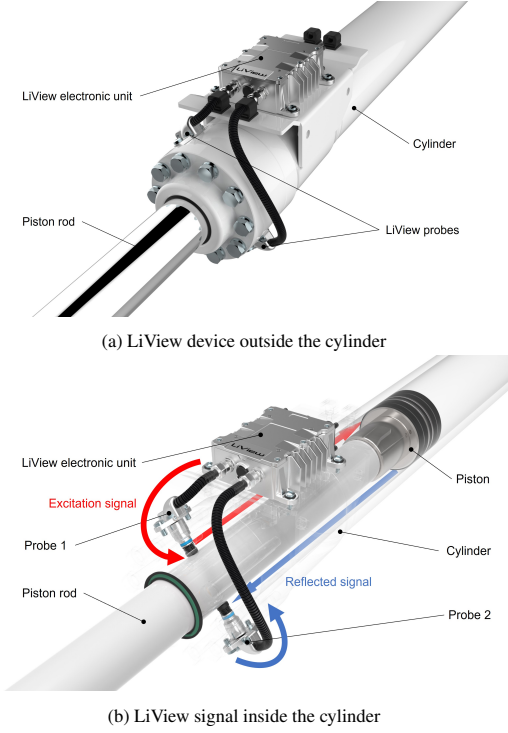


Figure 1: LiView device and signal. (a) illustrates a LiView device mounted outside a cylinder, with its probes connected to the cylinder structure. (b) shows the process of a measurement cycle of the LiView system, where the excitation and reflected signals are depicted as red and blue arrows, respectively. The LiView electronic unit first generates a microwave excitation signal, which is conducted through the black wire to probe 1 and capacitively fed into the cylinder there (the curved red arrow). The signal then propagates inside the oil between the piston rod and the cylinder until it hits the piston (the straight red arrow). Then, the signal is reflected by the piston and can be intercepted by probe 2 (the straight blue arrow). Finally, the signal is received by the LiView electronic unit (the curved blue arrow) and is processed there into the final measurement.

Port 1 and 2 correspond to probe 1 and 2 in Figure 1 respectively. They are connected to the LiView electronic unit via coaxial wires. When measuring, a stimulus is injected at Port 1, and its reflection is finally received by Port 2. Port 3 represents the cylinder tube with the piston moving inside, whose signal can't be measured by any probe. The cylinder structure among the three ports can be considered as the virtual transmission lines. In one measuring cycle, The LiView electronic unit first generates a signal at a predefined frequency and injects it into the cylinder structure through port 1. The injected signal passes from the cylinder bearing to the piston rod which is represented by port 3. It then propagates as electromagnetic waves through the oil inside the cylinder tube until it reaches the piston. The piston then reflects the signal, and the probe at port 2 can then detect

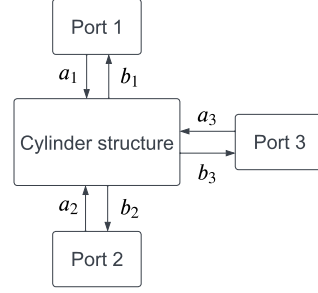


Figure 2: Flow-chart of the three-port electrical network of the LiView system and cylinder. Port 1 capacitively excites the signal, whose reflection can then be detected by port 2. Port 3 corresponds to the cylinder tube and the piston.

this reflected signal.

The quantities that are measured by the LiView electronic unit are the transmission t (at one specific frequency) between the exciting port 1 and receiving port 2 given by

$$t = \frac{b_2}{a_1}. \quad (4)$$

The piston position L , which is formally defined as the distance between the piston and its Bottom Dead Center (BDC) along the axial axis of the cylinder, determines the scattering parameters of the 3rd port:

$$a_3 = T(L)b_3, \quad (5)$$

with $T(L)$ modeling the cylinder as a transmission line. Under the assumption of reciprocity $S_{ij} = S_{ji}$, one can extract the relevant transmissions and reflections at ports 1 and 2 by combining Equations 3 and 5. Exemplary, the transmission t for a certain frequency as in Equation 4 for low frequency TEM-modes then reads (Braun et al., 2017-04-05)

$$t = S_{21} - \frac{S_{23}S_{13}}{S_{33} - \frac{1}{T(L)}}. \quad (6)$$

Note that all wave-related variables (E, a, b, S, t) in previous equations are complex numbers. With Euler's formula, it follows that any complex number z , with $r = |z|$ as its amplitude and $\theta = \arg(z)$ as its phase, can be written as

$$\begin{aligned} z &= re^{j\theta} \\ &= r \cos \theta + jr \sin \theta \\ &= \text{Re}(z) + j\text{Im}(z) \end{aligned} \quad (7)$$

where $j = \sqrt{-1}$ so that the real and imaginary part of z , $\text{Re}(z)$ and $\text{Im}(z)$, are both real numbers. Therefore, the data finally gathered by the LiView system are a complex-valued vector \mathbf{t} which has 121 elements corresponding to transmissions at the 121 frequencies, equally distributed in a range from 300 MHz to 1.5 GHz.

Our physical model for position detection is based on the electrodynamics of the cylinder tube given by Equation 6 and the derivation of $T(L)$ from Maxwell's Equations according to Braun et al. (2017-04-05). Specifically,

$$T(L) = e^{2L(-\epsilon'' + jk)}, \quad (8)$$

where ϵ'' represents the imaginary part of the complex-valued relative permittivity $\epsilon_r = \epsilon' + j\epsilon''$ and k refers to the angular wavenumber.

The existence of the relation $t = f(L)$ (an abstraction of Equations 6 and 8) paves the way towards a position detection method by solving the inverse $L = f^{-1}(t)$. Our physical model directly gives out the piston position by solving the inverse function. Looking at Equations 6 and 8, it's apparent that piston position L is nothing but a mathematical expression of the transmission \mathbf{t} , which can be measured by the LiView system, subjecting to scattering parameters of the three-port electrical network (Figure 2), the relative permittivity of the oil inside the cylinder, and the angular wavenumber. We assume all variables except the model input \mathbf{t} and output L are constants during inference and determine their values in advance. The scattering parameters S_{21} , S_{33} , as well as the product of S_{23} and S_{13} in Equation 6 are dependent on the specific cylinder structure and acquired by calibration via measurements or simulations of the respective cylinder. The relative permittivity ϵ_r , which quantifies the storage (real part) and dissipation (imaginary part) of the energy, can be obtained with the help of a Vector Network Analyzer (VNA). Since we know the frequency for each measurement cycle of the LiView electronic unit, we can easily get the angular wavenumber k from the equation $k = 2\pi f \sqrt{\epsilon' \mu_r} / c_0$ where f is the frequency, ϵ' refers to the real part of the relative permittivity, μ_r stands for the relative permeability which is approximately equal to 1 for oil and c_0 is the speed of light in vacuum. After all the calibrations, we could finally substitute the predetermined variables and the transmission \mathbf{t} measured by the LiView system during inference to solve the desired piston position L .

As long as the predetermined variables keep unchanged and the modeling of the coaxial cylinder structure remains accurate, the physical model performs well both in theory and in practice. However, the assumptions can surely break under harsh and irregular envi-

ronments. The oil permittivity ϵ is sensitive to environmental factors such as temperature, impurities in the oil, etc. The temperature effect is even more severe at extremely high or low temperatures. Because then, the change in permittivity of other materials such as the seals could break the assumption of the constant scattering parameters. To solve this issue within the domain of the physical method, we have to implement a mechanism for the physical model to decide when to use which calibrated scattering parameters. This method is however inaccurate, complicated to implement, and leads to noisy position values. Moreover, the coaxial structure is only a good approximation if the propagation length of the signal is long. As a result, when the piston is near the bottom of the cylinder tube or the piston rod bearing, the model assumptions of a coaxial cavity do not hold anymore and workarounds such as a switch to other models or look-up tables have to be implemented, which demand in-depth expert knowledge and impede a robust implementation that can easily be generalized to mechanically differing cylinder types. Then more elaborate and general models are needed for accurate position determination. Next, we will show how we found these more accurate models with better generalization performance by switching to learning-based methods.

4. Methods

We apply machine learning and deep learning-based approaches as a generic solution to cylinder piston position estimation by learning the underlying relationship between the input measurement and the target piston position, with the help of a large amount of data collected in a variety of work scenarios. Specifically, our goal is to learn the mapping relationship $L = f^{-1}(\mathbf{t})$ between the transmission \mathbf{t} measured by the LiView system and the desired piston position L by machine learning and deep learning methods. The original measurement data are 1D complex-valued vectors with 121 elements corresponding to the 121 equally distributed frequencies from 300 MHz to 1.5 GHz. Depending on the model architecture and the technology applied, we preprocess the raw measurement into the actual input to the model accordingly (sections 4.2, 4.3, and 4.4). The output of all models is always a scalar referring to the piston position recorded simultaneously when the input is measured.

This section introduces the general architectures of the models and specific methods we use to achieve our goal. we apply both the classical machine learning (section 4.1) and deep learning-based models (section 4.2

and 4.3), together with a novel technique named Frequency Encoding (4.4). The implementation details are given in section 5.2 and the model performance is analyzed in section 5.3.

4.1. Machine Learning Models

Random Forest (RF). Random Forest is a combination of tree predictors such that each tree depends on the values of a random vector sampled independently and with the same distribution for all trees in the forest (Breiman, 2001). To construct a RF, we first generate m new training sets from the original training set of size N and feature dimension d (with $d = 242 = 121 \times 2$ since we use real-valued model until section 4.3) by uniform sampling with replacement. This technique is also known as bootstrapping. For each sampled new training set, we randomly sample $d' = \lfloor \sqrt{d} \rfloor$ features and then train CART (Breiman et al., 1984) on the sampled feature subspace. Finally, all the trained CART are aggregated to form the RF, and the average prediction result of the trees is the final output. The process of bootstrapping and then aggregating is often abbreviated as bagging.

Gradient Boosted Decision Tree (GBDT). Another classical machine learning method based on the aggregation of decision trees is GBDT. The main difference between GBDT and RF is that the former uses boosting instead of bagging as in the latter. Boosting is a powerful technique for combining multiple 'base' classifiers to produce a form of a committee whose performance can be significantly better than any of the base classifiers (Bishop and Nasrabadi, 2006). In our case, we use DTs as base regressors and build an ensemble of them in a forward stagewise manner. At each iteration of the forward stagewise procedure, we train a DT to represent the negative gradient of the residual error from the previous iteration and aggregate to the ensemble by steepest descent.

RF and GBDT are both ensemble learner based on DTs. They utilize bagging and boosting respectively to overcome the tendency of overfitting and high variance in a single DT for better generalization performance. Given the excellent performance of both GBDT (Chen and Guestrin, 2016a; Dorogush et al., 2018; Ke et al., 2017) and RF (Breiman, 2001; Schonlau and Zou, 2020) on general regression problems, we adopted these two models for our task. However, these two models do not perform very well on our problem (section 5.3), especially compared to the deep learning-based models presented in the next section.

4.2. Deep Learning Models

Deep learning, or ANN, allows computational models composed of multiple processing layers to learn data representations with multiple levels of abstraction LeCun et al. (2015). Intricate patterns in large data sets can be implicitly discovered by exploiting backpropagation (Rumelhart et al., 1986) to change its internal parameter states. The motivation for the choice of deep learning is to use this mechanism to achieve better generalization performance since traditional machine learning methods are insufficient to learn complicated functions in high-dimensional spaces such as our case (with evidence given in section 5.3). The architecture of a deep learning model is a multilayer stack of simple modules (Figures 3, 4 and 5). In this section, we discuss the structure of our MLP, CNN, and CVNN models.

Multilayer Perceptron (MLP). MLP (Werbos and John, 1974; Rumelhart et al., 1986) is a feedforward ANN where every single neuron in adjacent layers is connected to each other. Because of the fully connected characteristic, MLP is also named as Fully Connected Neural Network (FCNN). The quintessential advantage of MLPs is that they are universal approximates provided sufficiently many hidden units (Hornik et al., 1989), i.e. they are able to represent a wide variety of functions requiring no special assumptions about the input. For the real-valued MLP (3a), we first concatenate the real and imaginary parts of a measured complex-valued transmission t to form a real-valued vector as the new input, and train real-valued MLPs to approximate the inverse function $L = f^{-1}(t)$ for prediction of the targeted piston position L . We evaluate MLPs with different numbers of hidden layers, each consisting of 32 neurons except the last one, which has 16 neurons. We also analyze the effect of four different activation functions, sigmoid, ReLU (Nair and Hinton, 2010), Leaky ReLU (Maas et al., 2013), and SELU (Klambauer et al., 2017), on MLPs.

Convolutional Neural Network (CNN). CNNs (LeCun et al., 1989) are a specialized kind of neural network for processing data that has a known, grid-like topology (Goodfellow et al., 2016). Units in a convolutional layer are organized in feature maps, within which each unit is connected to local patches in the feature maps of the previous layer through a set of weights (LeCun et al., 2015). The result of this locally weighted sum is then passed through the activation function like in MLPs to form the output feature map.

The motivation for CNN is its property that a convolutional layer should learn functions that represent local interactions in input. In our case, the local interactions are among neighboring frequencies. Based on the

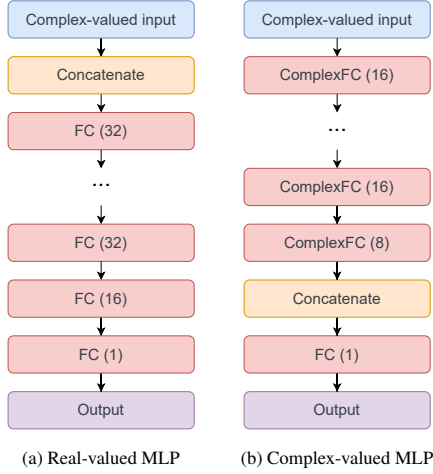


Figure 3: MLP architecture. The real-valued (a) and complex-valued (b) MLPs consist of Fully Connected (FC) and Complex-valued Fully Connected (ComplexFC) layers, respectively, with the number of units of a specific layer given in its following parentheses.

properties of electromagnetic waves, it is reasonable to assume that transmission t of adjacent frequencies are highly correlated, exhibiting local statistics which are easily detected. In section 5.3, we prove our hypothesis with training results and provide a credible explanation for the underlying physical mechanism.

As in real-valued MLP, we concatenated the real-valued real and imaginary parts of all 121 complex numbers to form the 1D grid with 242 elements as the input for our real-valued CNNs. Once we converted the complex-valued input to vectors with the shape of 1×242 , 1D local convolutional filters only to the frequency dimension (instead of the temporal dimension). A 1D CNN can then be constructed using these convolutional layers and trained to predict the targeted piston position. As depicted in Figure 4a, the first convolutional layer has a large kernel size (1×22) and stride (11). It's a common way to reduce dimensionality in frequency-based signal processing, e.g. in Supriya (2020). The first convolutional layer is followed by three convolutional layers with small kernels (1×3) and strides to extract informative features. Finally, a fully connected layer exploits those extracted features to make the prediction.

Note that we perform downsampling directly by convolutional layers, instead of max pooling layers, with a stride of more than one. The two ways result in a similar model structure considering the dimension of the feature maps of each layer and are experimentally proved in section 5.3 to have similar effects on generalization performance for our project. We prefer the latter from

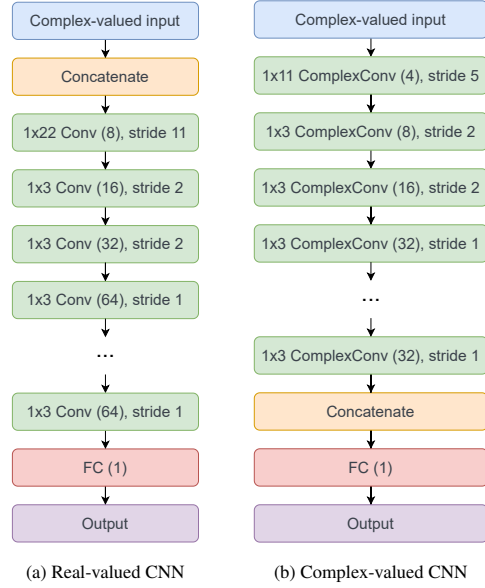


Figure 4: CNN architecture. The backbone of the real-valued (a) and complex-valued (b) CNNs is 1D convolutional (Conv) and 1D complex-valued convolutional (ComplexConv) layers, respectively. For each layer in the illustration, the kernel size is presented as the first term of the description text and the number of output channels is given in parentheses. Different strides are used for downsampling. At the end of all CNNs, there is always a Fully Connected (FC) layer to map the features extracted by Conv or ComplexConv layers to the desired output. In practice, we modify the number of convolutional layers so that each model has around 10K parameters.

the perspective of intuitive comparisons between real-valued and complex-valued CNN, described in the next section.

4.3. Complex-Valued Neural Network (CVNN)

CVNNs are ANNs that operate in complex space with complex-valued input and weights. The main reason for their advocacy lies in the difference between the representation of the arithmetic of complex numbers, especially the multiplication operation (Bassey et al., 2021). Figure 5 illustrates our implementation of the complex-valued operation inside a layer of a CVNN. In the illustration, $Re(X)$ and $Im(X)$ refer to the real and imaginary parts of a complex-valued input, while $Re(W)$ and $Im(W)$ refer to the real and imaginary parts of the layer weight. To imitate the multiplication of complex numbers, we first split the real and imaginary parts of the complex-valued input and weight as stated, then calculate the components $Re(X) * Re(W)$, $Re(X) * Im(W)$, $Im(X) * Re(W)$, and $Im(X) * Im(W)$ separately, and lastly additively combine these four products to construct a new complex-valued output of the specific layer with the real part as $(Re(X) * Re(W) - Im(X) * Im(W))$ and

the imaginary part as $(Re(X) * Im(W) + Im(X) * Re(W))$. Once the complex-valued outputs are obtained, a split activation function (Bassey et al., 2021) is applied to them, where the real and imaginary components of the signal are independently input into a chosen real-valued activation function.

Note that the symbol $*$ here does not have to refer to the multiplication operation. One can easily switch the multiplication operation to the convolution operation. In this case, X will refer to complex-valued feature maps from the last layer and W the complex-valued kernels of a convolutional layer. Accordingly, $Re(X)$ and $Im(X)$ (or $Re(W)$ and $Im(W)$) each represent half of the feature maps (or kernels). A great illustration of the operation of a complex-valued convolutional layer can be found in Trabelsi et al. (2018). Furthermore, we can extend the meaning of $*$ to an arbitrary function evaluation. In this case, $Re(W)$ and $Im(W)$ are the functions in the same form but with different coefficients. They take either $Re(X)$ or $Im(X)$ as input and the outputs are denoted as the four blocks in the second row of Figure 5.

Inspired by Matthès et al. (2021) and Trabelsi et al. (2018), we implement the $Re(W)$ and $Im(W)$ as two standard real-valued layers respectively but combine their outputs in the way stated above to construct a CVNN instead. If we denote the We denote the implementation of complex-valued counterparts of FC() and Conv() as ComplexFC() and ComplexConv() (in Figures 3 and 4), with the number of neurons for FC layer or kernels for Conv layer in their real-valued layers given in the following parentheses. For example, a ComplexFC(16) layer is implemented by two FC(16) layers representing $Re(W)$ and $Im(W)$, respectively.

The choice of CVNN is motivated by the fact that the input is complex numbers, where the real and imaginary parts, or more specifically their amplitude and phase, are statistically correlated. This information will be lost if we simply choose to represent a complex number as an ordered pair of two real numbers, as in the previous sections. CVNN can reduce the ineffective degree of freedom in learning or self-organization to achieve better generalization characteristics (Hirose, 2012). The mechanism of CVNN can also be seen as applying an infinitely strong prior to the original MLP and CNN forcing them to operate in the complex domain. This could be (and is proved in section 5.3 to be) useful since we’re giving the models more information about the real-world application. Guided by this idea, we further introduce another technique named Frequency Encoding.

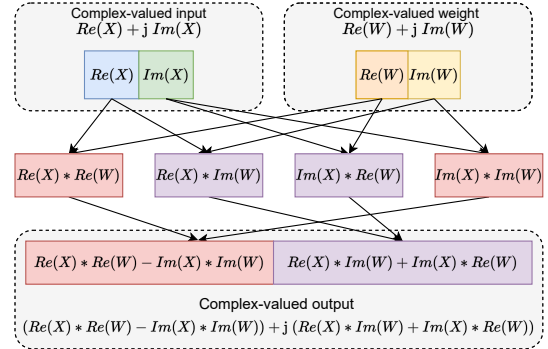


Figure 5: An illustration of one layer in a CVNN. Both the input and the output are complex numbers. Layers in CVNN mimic calculations in the complex domain. The symbol $*$ in the figure represents multiplication for ComplexFC layer and convolution for ComplexConv layer.

4.4. Frequency Encoding (FE)

FE encodes the (normalized) frequencies f for each channel of the complex-valued input, and then the code c is added element-wise to the input after weighting by a learnable parameter w . Formally, the FE pipeline in this paper can be expressed as:

$$\begin{aligned}
 c &= w * f, \\
 Re(x') &= Re(x) + c, \\
 Im(x') &= Im(x) + c,
 \end{aligned} \tag{9}$$

where x' and x are the encoded and original 1D input vector, respectively. Both consist of 121 elements corresponding to the 121 frequencies. As illustrated in Figure 6, the 121 frequencies from 300 MHz to 1.5 GHz are uniformly scaled to $[0,1]$ at first. The normalized frequency vector is denoted as f . Then the uniformly encoded frequencies f are multiplied by the corresponding learnable weights to generate the code c . Note that the weights w for frequency encoding are learned by back-propagation during training, just like any other learnable parameters in the model. After that, the code for each frequency is added to both the real and imaginary parts of the original input x (in our case the measured transmission t) at the corresponding frequency, forming the new input under FE x' to the models.

FE injects the information about the exact frequency of the electromagnetic waves that the sensor operates on directly into the model. Frequency information should (and in section 5.3 proved to be) helpful because the precise value of the frequency will significantly affect the corresponding transmission t , and furthermore, the piston position. Since we cannot precisely confirm a priori the impact of each frequency, the learnable weights are

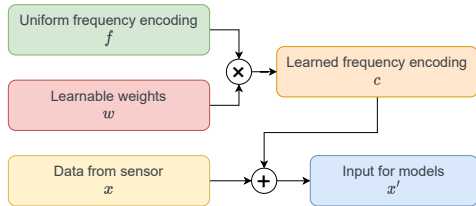


Figure 6: Sketch of the Frequency Encoding (FE) procedure. The normalized frequencies f are multiplied with the learnable weights w which leads to the code c . This c then serves as an additive bias for the original model input x . Therefore, the frequency information is encoded and injected to the final input for models x'

introduced to correct the initial uniform encoding. We prefer FE over intuitive concatenation, mainly for the following reasons. Firstly, it uses the summation of corresponding elements to avoid the explosion of the input dimension and further the model parameters. Secondly, the frequency information is accurately introduced into the correct corresponding input element instead of letting the model find the correspondence between the two by training itself. Another advantage of FE is that it's also a model-agnostic technique, i.e., we can easily apply it to any learning-based models benefiting from backpropagation without any particular change of the model structure. It turns out that FE significantly affects model performance. More details about the evaluation results can be found in section 5.3.

5. Experiments

5.1. Dataset

Experimental Configuration. Our experiments for the measurement of the transmission t and the recording of the piston position L are carried out at a wide variety of temperatures in the range from 25 °C to 95 °C. In all experiments, a LiView device is mounted on the same hydraulic cylinder with a stroke of 1815 mm and keeps measuring transmissions at 121 frequencies uniformly distributed in a range from 300 MHz to 1.5 GHz as described in section 3. A hydraulic power unit drives the cylinder, and a magnetostrictive position measuring system measures the piston position. Other than the input and output for the models, metadata such as operating frequency, cylinder temperature, and timestamps are also recorded. Three typical experiment recordings are shown in Figure 7. As we can see from the three graphs on the left side of Figure 7, typical piston movements are uniform linear motions shown as straight lines in the figures. To test the performance under different working conditions, we also adopt varying speed profiles by mixing end-to-end and jittering movements at

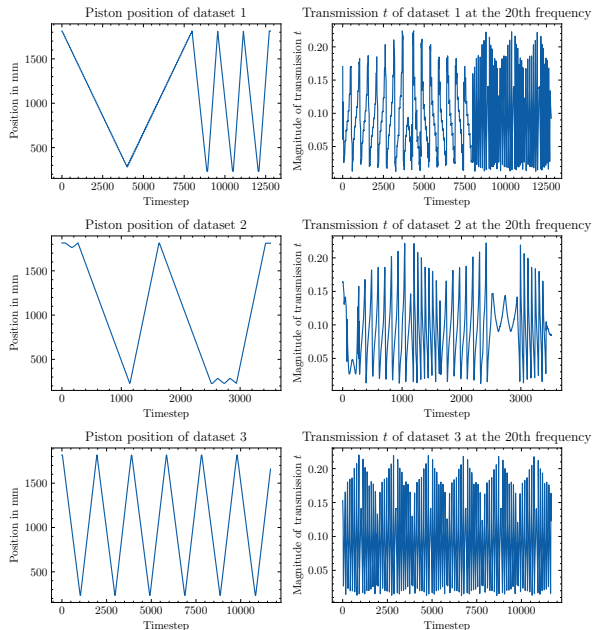


Figure 7: Position and S21 parameters from three typical datasets. Each row represents one dataset, with its piston position profile showing on the left and the complex magnitude (or amplitude) of the measured transmission at the 20th frequency on the right.

different speeds during different experiments, shown respectively in different slopes of lines in the upper left and the zigzag patterns in the middle. The amplitudes of the corresponding measured input are drawn on the right side of Figure 7. It's evident that the transmission t changes with the piston position L , which verifies our assertion of the existence of $t = f(L)$.

Dataset Split. The core idea behind our dataset split is that we selected two test sets deliberately in two different ways to test which one reflects the true generalization ability of our models. We generated 534K data pairs (t, L) among 73 experiments in total, where t is a 1D vector with 121 complex-valued elements corresponding to transmissions at 121 frequencies and L stands for the targeted piston position. We randomly split the data from 68 datasets at a ratio of 80 to 20 for the training and the first test set. There is also a second test set composed of the remaining five datasets. To distinguish the two test sets, we named them "test set from random split" and "test set from new datasets" (since the latter one is "new" to the training set) in Figure 8, respectively. The final ratio of the data volume in three datasets is 10/2/1 (training/test1/test2).

We split the data this way to show that only the second test set, "test set from new datasets", is the only suitable set to test generalization. As can be seen from

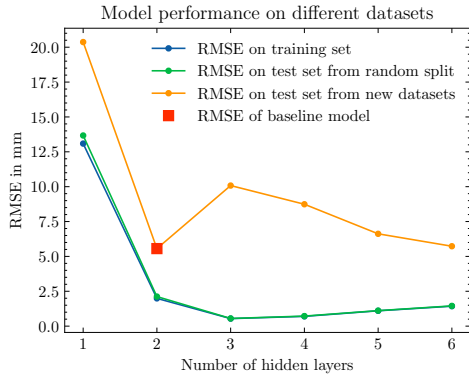


Figure 8: Performance of MLP models with different numbers of hidden layers on different datasets

Figure 8, the performance of all MLP models on the first test set, "test set from random split", is almost identical to the performance on the corresponding training sets. We argue that, although both test sets are kept unseen from the training process, the "test set from the random split" shares too many influential factors with the training set since they are from the same experiments, which makes the data in the two not quite the same but very close. These influential factors could be explicit ones such as speed profile and temperature, or implicit ones like chamber pressure, oil quality, parts aging effect, etc. The second test set, consisting of complementary datasets, doesn't suffer from the issue and therefore is the only suitable test set that reflects the actual generalization performance. That said, the test set from the random split is not entirely useless. It is still an indicator to show what will happen if there are only slight changes, which was helpful in the model selection phase and could help if we could cover a broader range of working conditions of the cylinder. But in the following sections, unless otherwise specified, we refer to "the test set" as the one from the new datasets.

5.2. Implementation Details

This section describes the implementation of the models introduced in section 4 and the training details.

Since the input for our models are 1D vectors with 121 complex-valued elements, we treat them for both classical machine learning models and real-valued ANNs as real-valued input with 242 features by concatenating their real and imaginary parts. On the other hand, CVNNs can use the measured data with 121 complex-valued features off-the-shelf. We also tried to represent complex numbers using magnitude and phase, but the final results of the two ways to handle complex

numbers were almost indistinguishable. Frequency Encoding was also applied to the models as stated in section 4 by choice.

To preserve the possibility of running the model on an edge computing device and integrating it into the current LiView electronic unit in the future, we limited the total parameters for each model to just under 10K.

We utilized the scikit-learn (Pedregosa et al., 2011) implementation of random forest regressor. For GBDT, we used LightGBM (Ke et al., 2017), which can in theory significantly outperform XGBoost (Chen and Guestrin, 2016b), another popular implementation of GBDT, in terms of computational speed and memory consumption according to Ke et al. (2017). For both RF and GBDT, we fine-tuned the hyperparameters in 500 trials sampled by TPE (Tree-structured Parzen Estimator) algorithm in a large hyperparameter space which covered both shallow and deep models with the help of the hyperparameter optimization framework Optuna (Akiba et al., 2019). The test performance of both models with the best hyperparameter set is given in Table 1.

We also trained all ANNs, implemented by PyTorch 1.12 (Paszke et al., 2019), using the hyperparameters acquired by fine-tuning in 500 trials with the help of Optuna. It turned out that the best hyperparameter sets for MLP, CNN and CVNN were very similar. Accordingly, we chose the final hyperparameters as the following. At the beginning of the training process, we always initialized the biases to zeros and the weights using Xavier uniform random initialization procedure (Glorot and Bengio, 2010). For training, we used the AdamW optimizer (Loshchilov and Hutter, 2017a), which is the combination of the classical Adam (Kingma and Ba, 2017), with $\beta_1 = 0.9$ and $\beta_2 = 0.999$, and the decoupled weight decay regularization of which we set the coefficient to 10^{-4} . We chose the learning rate of 10^{-3} and a learning rate scheduler that linearly decreased the learning rate starting at half of the fixed total epochs from 10^{-3} to 0. This simple learning rate was proved to achieve better generalization compared to no scheduler or delicate ones such as cosine annealed warm restart scheduler (Loshchilov and Hutter, 2017b) for all models. The batch size was set to 128 for MLPs and 64 for CNNs. We also applied Batch Normalization (BN) (Ioffe and Szegedy, 2015) to some models (Tables 2 and 3) and early stopping mechanism to all models. Another regularization we tested was Dropout (Srivastava et al., 2014), but it did not help the generalization in all our trials. We also compared four activation functions (sigmoid, ReLU, Leaky ReLU, and SELU) under the same model structure and went along only with the best-performing one, sigmoid, after the comparison (section

5.3).

We trained our models on a Ubuntu workstation with NVIDIA GeForce RTX 3090, AMD Ryzen 9 3950X, and 64 GB DDR4 RAM. The evaluations (section 5.3) were conducted on the same workstation. To validate the performance of our model on edge computing devices, we also tested the inference speed on the CPU of a Jetson Xavier NX with the lowest power mode (10 W, 2 cores).

5.3. Model Comparison

A detailed discussion of the evaluation results and analysis can be found in this section. We use Root Mean Squared Error (RMSE) on the test set as the major criterion for our analysis of model performance. To facilitate the assessment of the model performance by other standards in the industry, we also provide test Mean Error (ME) and Mean Absolute Error (MAE) for some models. RMSE, ME and MAE are all given in millimeter. Accordingly, we calculate the Relative Error (RE) as the ratio between RMSE and the stroke of the cylinder 1815 mm. Since the ME of our models are all close to 0, the more commonly used error expression in industry, which is $ME \pm \text{standard deviation}$, can be approximated as $ME \pm RMSE$ in our case.

Baseline Model. We started our analysis by setting up the baseline model. In consideration of the pervasiveness and flexibility of MLPs, we trained MLPs with different numbers of hidden layers with sigmoid activation function but without applying Batch Normalization and Frequency Encoding at first. The evaluation results based on RMSE are given in Figure 8. Note that only the RMSE on the test set from new datasets is the proper indicator of the generalization performance (as described in section 5.1). Looking at the test set performance shown in the orange curve in Figure 8, it is apparent that increasing the depth of the model further after two hidden layers surprisingly brings down the model performance. Similar observations were also reported in (He and Sun, 2014; Zeiler et al., 2013; Simonyan and Zisserman, 2015), where aggressively increasing the depth leads to saturated or degraded accuracy. Since two-hidden-layer MLP already provided the best generalization performance, we chose the two-hidden-layer MLP as the baseline.

It’s also worth mentioning that we also kept computational resources in mind when choosing the baseline. Although a high-end GPU (NVIDIA 3090) currently did all the training and analyses, we plan to deploy the model on an edge computing device or on a real-time platform in the future. In fact, the two-hidden-layer MLP is not necessarily always the best-performing

model without computational limitations. One argument is that the shape of the test performance curve in Figure 8 is a good match for the double-descent risk curve in Belkin et al. (2019), which indicates that introducing more hidden layers could lead to even lower RMSE on the test set. Another clue lies in the training error. Except for the fact that it almost overlapped with the curve of “RMSE on the test set from random split” as explained in section 5.1, the training error slightly rises rather than falls once the model size exceeds three hidden layers. This phenomenon where the training error increases as the model gets bigger and deeper is the degradation problem reported in He et al. (2015) and Srivastava et al. (2015). The degradation problem could be solved by techniques such as residual learning reformulation (He et al., 2015). However, considering the tradeoff between the computational burden and model performance, as well as the fact that even this simple baseline already outperforms the traditional physical model (section 5.3), we still prefer the two-hidden-layer MLP as the baseline. To make the comparisons among the models below and the baseline fair, we limited the parameter numbers of all the following models to a roughly equivalent range of about 10K. Based on this guiding principle, we chose the real- and complex-valued CNNs as illustrated in Figure 4 and discussed in section 4. **Baseline vs Classical.** We first compare the

Framework	train RMSE	test RMSE	RE(%)
MLP(baseline)	1.99	5.56	0.31
Physical model*	-	13.61	0.75
RF	0.89	44.35	2.44
GBDT	4.77	38.56	2.12

* We evaluated the traditional physical model only on the test set since it doesn’t need a training process (so its training RMSE is left blank). The RMSE of 13.61 mm, which corresponds to a RE of 0.75%, is the average performance of the physical model on the test set.

Table 1: Performance comparison of baseline Multilayer Perceptron (MLP) (deep learning), Random Forest (RF) and Gradient Boosted Decision Tree (GBDT) (classical machine learning), as well as the traditional physical model. For each model, the performance is represented as Root Mean Squared Error (RMSE) on the training and test set. The Relative Error (RE), which is the ratio between test RMSE and the cylinder stroke, is also listed.

baseline MLP model with the traditional physical model (Braun et al., 2017-04-05) and classical machine learning models described in section 4.1.

The physical model generally performs well in a mild and stable environment. However, its accuracy drops when dealing with our complex working scenarios and a wide range of temperature changes. We tested the per-

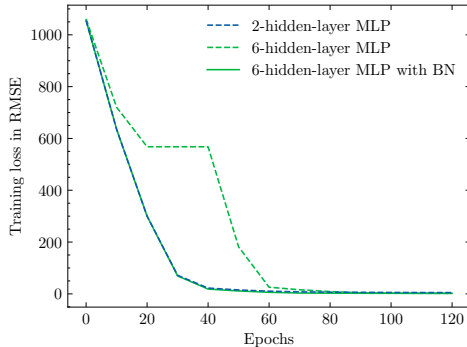


Figure 9: Training loss versus epochs for Multilayer Perceptron (MLP) models with different numbers of hidden layers. The deep (6-hidden-layer) model suffers from an unstable training process due to the vanishing gradient issue. Batch Normalization (BN) help eliminate this problem, bringing the training of the deep model back to the normal situation, shown as the training process of a shallow model (2-hidden-layer MLP).

formance of the physical model on the test set and calculated an average RMSE of 13.61 mm obtained from measurements ranging from room temperature up to 84 °C. For a cylinder stroke of 1815 mm, it corresponds to an RE of 0.75%, which is outperformed by the baseline model with a test RMSE as 5.56 mm.

Both RF and GBDT suffer from poor generalization behavior in our case, which can be inferred from the massive gap between the train and test RMSE, especially for RF. The performance of GBDT is inferior to our baseline MLP or even the traditional physical model. Considering that the models for both frameworks are already the best choice after extensive hyperparameter fine-tuning with 500 trials each, we thus confirm our hypothesis that it’s the lack of well-designed features with domain knowledge that makes it difficult for classical machine learning methods to obtain comparable performance on our piston position task using scattering parameters. Thereafter we turned our attention to deep learning and only adapted ANN models to enhance their performance.

Batch Normalization (BN). The first technique we applied to the baseline model was BN (Ioffe and Szegedy, 2015). As can be seen from the first two lines of Table 3, it helps improve the test RMSE by 30% from 5.56 to 3.89 mm. However, this is not the case for CNN, CVNN, or models with Frequency Encoding which hardly benefit from BN in our case.

Another point worth mentioning is that BN does help stabilize the training process for deep MLPs. As can be seen in Figure 9, the 6-hidden-layer MLP without BN cease to advance for more than 20 epochs by showing

a long plateau of training errors likely to be caused by vanishing gradients, especially for deeper models, while BN eliminates this phenomenon, since it ensures forward propagated signals to have non-zero variances and therefore healthy norms of gradients during backpropagation.

Activation Functions. The choice of activation functions in deep networks has a significant effect on the training dynamics and task performance (Ramachandran et al., 2017). Table 2 compares the generalization performance (ME, MAE, RMSE, and RE on the test set) of 2-hidden-layer batch-normalized MLPs with four different activation functions. Previous research such as Glorot et al. (2011) shows that ReLU generally performs better in most deep learning models, especially for image and text data. In our case, it converges faster too, but can not provide promising results in our case. Its variant, Leaky ReLU, exhibits similar behavior. Sigmoid, on the other hand, outperforms other activations. We believe this intriguing result is attributed to the fact that the sigmoid function, $f(z) = 1/(1 + \exp(-z))$, is more in line with the physical characteristic of the input transmission t expressed in Equations 7 and 8 since exponential function dominates. Components that are better reflections of the real physical world allow models to learn the relationship $L = f^{-1}(t)$ better, especially for shallow ANN modes like our baseline, where the representation learning ability is restricted by the depth and parameters of the model. This assumption also explains why SELU, a half-linear-half-exponential function, comes in between the more exponential sigmoid and the more linear ReLU. Because of the excellent performance of the sigmoid activation, we adopted it for all the following models.

Ablation Study. Evaluation results of MLPs and CNNs are provided in Table 3. The top and bottom parts of the table show models in these two frameworks separately. For models in both frameworks, Batch Normalization (BN), Frequency Encoding (FE), and Complex-Valued Neural Network (CVNN) were applied to them selectively. We kept only the promising models and omitted poorly performing ones. Since BN doesn’t perform well along with the other two techniques in our test, we always applied FE and CVNN without BN. In the following paragraphs, we first focus on the MLP part of the table to discuss the outcome of FE and the impact of CVNN. Finally, we compare MLP and CNN and relate the model performance to the physical characteristic of our data.

Frequency Encoding (FE). This simple technique is able to reduce the test RMSE by more than half from 5.56 to 2.5 mm, as shown by the first and the third row

Framework	BN	Activation	ME	MAE	RMSE	RE(%)
MLP	✓	Sigmoid	-0.18	2.08	3.89	0.21
MLP	✓	SELU	-0.08	4.3	5.88	0.32
MLP	✓	ReLU	-0.06	4.00	5.96	0.33
MLP	✓	LeakyReLU	0.00	4.79	8.3	0.46

Table 2: Performance comparison for models with different activation functions. All models in the table are 2-hidden-layer real-valued MLPs with Batch Normalization (BN). The only difference is their activation functions.

Framework	BN	FE	CVNN	ME	MAE	RMSE	RE(%)
MLP (baseline)				-0.1	2.04	5.56	0.31
MLP	✓			-0.18	2.08	3.89	0.21
MLP		✓		-0.11	1.24	2.5	0.14
MLP			✓	-0.07	0.95	1.53	0.08
MLP		✓	✓	-0.07	0.75	1.23	0.07
CNN				0.34	1.27	2.32	0.10
CNN	✓			0.82	1.69	2.35	0.13
CNN		✓		0.11	0.8	1.47	0.08
CNN			✓	0.45	1.02	1.53	0.08
CNN		✓	✓	0.18	0.74	1.01	0.06

Table 3: Performance comparison for models with different architectures. Both frameworks, MLP (Figure 3) and CNN (Figure 4) are tested with techniques Batch Normalization (BN) and Frequency Encoding (FE). Check marks in the Complex-Valued Neural Network (CVNN) column mean that we adopted complex-valued Multilayer Perceptron (MLP) (Figure 3b) or complex-valued Convolutional Neural Network (CNN) (Figure 4b) for the model in that specific row. The model performance is shown by Mean Error (ME), Mean Absolute Error (MAE), Root Mean Squared Error (RMSE) and Relative Error (RE) based on RMSE.

of Table 3. As stated in section 4.4, we apply FE with learnable weights in a multiplicative way and add the weighted codes to the original input. This also means the significant improvement by FE was achieved by just adding $121 \times 2 = 242$ parameters to our baseline, which is a model with about 10K parameters in total. In other words, FE boosts the model performance by 55% at the cost of merely 2% of more parameters. This result strongly supports our hypothesis that providing the model with frequency information will significantly improve the model’s performance. It also suggests that we should build learning-based models as physically close to the real-world application as possible. As a side note, we also tested a variant of the standard positional encoding, which encodes the frequency by sinusoidal functions and directly adds to the input without any weighting process. This mode only slightly improves the model performance compared to the baseline. The reason lies in the fact that we are not able to determine in advance the specific effect of frequency on the input. Modeling this impact by a blindly chosen function, which only makes the frequencies unique instead of informative, turns out not to be a good design. Thus, we prefer the implementation with learnable weights.

Complex-Valued Neural Network (CVNN). Be-

sides real-valued MLPs (with architecture illustrated in Figure 3a and performance given in the first three rows of section 3), Table 3 also displays the test performance of complex-valued MLPs (with structure depicted in Figure 3b) indicated by check marks in the column CVNN. As discussed in section 4.2, one layer of our CVNN model consists of two standard layers representing the real and imaginary parts of complex-valued weights, respectively. We combine them in a way to mimic the calculation of complex numbers. To ensure fairness in comparing complex-valued and real-valued models, we carefully adjusted the depth and width for each CVNN so that their total number of parameters was close to their real-valued counterparts (see section 5.4). We conjecture that the CVNN helps with the model performance due to the complex-valued characteristic of the model input and traditional physical model we would like to approximate. We confirm our hypothesis by comparing the first and fourth rows of the Table 3. The complex-valued 2-hidden-layer MLP significantly cuts down the test RMSE by over 72% to 1.53 mm. This improvement comes only at a price of about 7% of more model parameters.

Incorporating FE into CVNN can further enhance model performance. As a result, the integration of these

two components leads to the best performance for models based on the MLP framework. The test RMSE drops by 78% to 1.23 mm while the model is only 9% bigger than the baseline. Compared to the fact that we have known from Figure 8 that stacking layers blindly is, instead of an upgrade, but a downgrade of the model performance, the achievement by FE and CVNN is undoubtedly phenomenal.

MLP vs CNN. Compared to MLP, CNN is a better framework for our task. First, the enhancement due to Frequency Encoding and CVNN on CNN is in line with the progress they made on MLP. What really stands out about CNNs (as listed in the Table 3) is that their overall performance is consistently better than that of MLPs in all cases. We believe the superiority of CNN has two main reasons. Firstly, it is for the sake of the parameter sharing mechanism of CNN, which enables it to contain more layers with the same number of model parameters. Therefore, limiting the number of model parameters results in the fact that CNNs are able to take advantage of the extra depth. A deeper architecture provides an exponentially increased expressive capability and is more likely to learn rich distributed representations (Rumelhart et al., 1986) of data, which is beneficial to the regression task of the final layer. More importantly, local connections between the frequencies also play an essential role here. For example, the position of the piston will have a local effect on the frequency spectrum of the input transmission t . As shown in Figure 10, the shape and form of the peaks and valleys in the spectrum are different when the corresponding piston position changes. We know from the physical model that the damping of the peak is frequency-dependent, and the location of the peak hinges on the piston position. Those local changes of peak patterns can be easily detected by a CNN since its feature maps for each layer only focus on local patches.

The best model. Finally, we propose our best-performing model: the complex-valued CNN with Frequency Encoding. It manages to reduce the test RMSE by 82% compared to the baseline MLP model. This achievement is entirely attributable to model design based on the physical characteristics of the system. We hope this will remind researchers working on projects related to scattering parameters to focus on the design of the deep learning model rather than simply adopting the standard model. Physical models remain at the core of the field, but the direct computation of physical quantities through equations that are not suitable for all scenarios may no longer be the optimal solution. Compared to the RMSE given by the traditional physical model, our dedicated best-performing deep learning

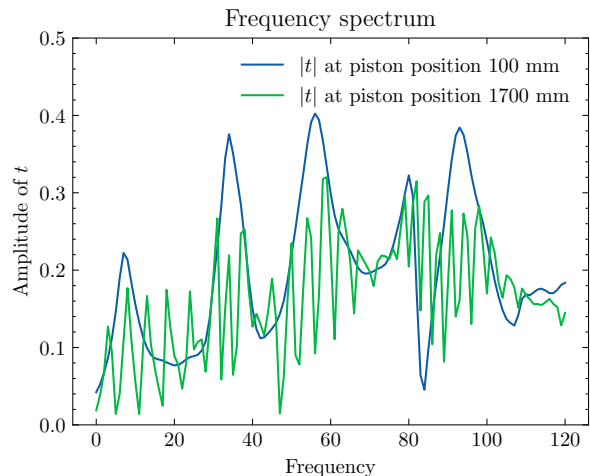


Figure 10: Frequency spectrum of transmission t at two different piston positions. The amplitudes of model input t at the shown two positions show clearly different local patterns, which are assumed to be easily detected by a CNN.

model exhibits a reduction by a factor of 1/12, demonstrating a substantial improvement in accuracy and robustness considering the diversity of the datasets.

5.4. Model complexity

While the previous sections focus on the model performance in terms of accuracy, in this section we shift our attention to speed and complexity. All test results regarding model complexity are given in Table 4. As previously mentioned, we intentionally limit the parameters of the model to 10K to preserve the potential for deployment on an edge computing device. The number of parameters for our deep learning models is specified in the fourth column of Table 4. Note that our most accurate model (in the last row) has slightly more parameters than the other models. However, this is not the reason for its superior accuracy. As shown in Figure 8, blindly stacking model parameters can deteriorate the model performance. This is also the reason that the baseline MLP only has 8K parameters, as the 10K version was found to be less accurate. Therefore, the enhancement should be attributed to better model design considering the physical characteristics of the system, i.e. CNN, FE, and Complex-Valued Neural Network, rather than the extra parameters.

The training speed is recorded on an NVIDIA GeForce RTX 3090 and in the form of seconds per epoch with each epoch containing 411K data points. We note that the training time for CNN is longer than MLP. This is because that CNN with the same parameters will perform more operations than MLP be-

Framework	FE	CVNN*	Params (K)	Training (s/epoch)	Inference ₃₀₉₀ (μ s)**	Inference _{NX} (μ s)**
MLP			8	8		6
MLP	✓		9	9		7
MLP	✓	✓	9	18	$\approx 2 \times 10^{-5}$	27
CNN			9	32		77
CNN	✓		9	33		95
CNN	✓	✓	10	65		161

* Instead of adopting torch.complex64 directly for the implementation of CVNNs in this table, we used two torch.float32 tensors to replace the real and imaginary parts of a torch.complex64 weight, respectively. We found that torch.complex64 significantly reduces the training and inference speed.

** $1 \mu\text{s} = 1 \times 10^{-6} \text{ s}$

Table 4: Model complexity for proposed deep learning models. The number of model parameters, training, and inference speed of MLP and CNN models with their Frequency Encoding (FE) or Complex-Valued Neural Network (CVNN) variants are listed. The number of parameters for all models is kept around 10K by design. The training speed is recorded on an NVIDIA GeForce RTX 3090 and in the form of seconds per epoch with each epoch containing 411K data points. The inference speed is tested on the same RTX 3090 (the second to last column) and in addition on the CPU of Jetson Xavier NX in the lowest power mode (the last column).

cause of CNN’s parameter-sharing mechanism. Similarly, CVNN is slower than real-valued ANN due to extra computation and IO cost for the complex domain (Figure 5). Also, note that the low-level implementation of data type could also lead to different training speeds. We implemented CVNN both in ”torch.complex64” and ”torch.float32”. The former can directly implement a complex-valued tensor, and the latter replaces the real and imaginary parts of a complex-valued tensor with two real-valued tensors. The two implementations are mathematically equivalent, but we find that torch.complex64 significantly reduces the training and inference speed (e.g. for about 50%, from 65 to 94 s/epoch for the training time on RTX 3090 and from 161 to 243 μ s for the inference time on Jetson Xavier NX, in the case of the CNN framework in the last row).

We also tested the inference speed of our models. Our test results on the 3090 were unstable and convergent, as the speed of the calculations was too fast, leading to too pronounced random fluctuations. Our test results on all models are around $2 \times 10^{-5} \mu\text{s}$. To represent the potential of the model to operate on edge computing devices, we tested the inference speed on the CPU of a Jetson Xavier NX at the lowest power mode (10 W, 2 cores). Here, the inference time demonstrates a similar pattern to the training time since they are both strongly influenced by the actual operations performed in the hardware. Note that the unit of the inference speed is microsecond μs where $1 \mu\text{s} = 1 \times 10^{-6} \text{ s}$. This implies that even the slowest model is capable of performing more than 6000 inferences per second, sufficient for real-time applications.

6. Conclusion

In this paper, deep learning models were proposed and evaluated for the piston position detection task inside a cylinder. The input to our models, which is measured by a device named LiView, is a mathematical expression of scattering parameters of a three-port network. The training and test set are carefully chosen to accurately reflect the generalization performance of our models. Considering the possibility of future integration of our model into the LiView electronic unit, the number of parameters was restricted to about 10K for all models. It is demonstrated that deep learning models (MLP and CNN) consistently outperformed classical machine learning methods (RF and GBDT) and the traditional physical approach. Further improvements were made by incorporating Frequency Encoding and CVNN to the deep learning models, resulting in 55% and 72% improvement in generalization performance at the cost of merely 2% and 7% extra model parameters, respectively. The best-performing model consisting of the three winning components, a complex-valued CNN with FE, managed to plummet the error to hardly 1/12 compared to the traditional physical model.

The potentials of combining deep learning and scattering parameters are far from being limited to the position detection task. We plan to extend the paradigm to predictive maintenance and investigate oil permittivity problems. We are excited about the future of a deep learning-based LiView.

References

Akhavanhejazi, M., Gharehpetian, G., Faraji-dana, R., Moradi, G., Mohammadi, M., Alehoseini, H., 2011. A new on-line moni-

- toring method of transformer winding axial displacement based on measurement of scattering parameters and decision tree. *Expert Systems with Applications* 38, 8886–8893. doi:10.1016/j.eswa.2011.01.100.
- Akiba, T., Sano, S., Yanase, T., Ohta, T., Koyama, M., 2019. Optuna: A Next-generation Hyperparameter Optimization Framework. doi:10.48550/arXiv.1907.10902, arXiv:1907.10902.
- Bader, O., Haddad, D., Kallel, A.Y., Hassine, T., Amara, N.E.B., Kounoun, O., 2021. Identification of Communication Cables Based on Scattering Parameters and a Support Vector Machine Algorithm. *IEEE Sensors Letters* 5, 1–4. doi:10.1109/LSENS.2021.3087539.
- Barbosa, D.C.P., Tarrago, V.L., de Medeiros, L.H.A., de Melo, M.T., da Silva Lourenco Novo, L.R.G., Coutinho, M.d.S., Alves, M.M., Lott Neto, H.B.D.T., Gama, P.H.R.P., dos Santos, R.G.M., 2019. Machine Learning Approach to Detect Faults in Anchor Rods of Power Transmission Lines. *IEEE Antennas and Wireless Propagation Letters* 18, 2335–2339. doi:10.1109/LAWP.2019.2932052.
- Bassey, J., Qian, L., Li, X., 2021. A Survey of Complex-Valued Neural Networks doi:10.48550/arxiv.2101.12249, arXiv:2101.12249.
- Belkin, M., Hsu, D., Ma, S., Mandal, S., 2019. Reconciling modern machine-learning practice and the classical bias–variance trade-off. *Proceedings of the National Academy of Sciences* 116, 15849–15854. doi:10/gf5dmw.
- Bertolini, M., Mezzogori, D., Neroni, M., Zammori, F., 2021. Machine Learning for industrial applications: A comprehensive literature review. *Expert Systems with Applications* 175, 114820. doi:10.1016/j.eswa.2021.114820.
- Bishop, C.M., Nasrabadi, N.M., 2006. *Pattern recognition and machine learning*. volume 4. Springer.
- Braun, S., Engler, A., Cremer, R., Nannen, I., 2014-01-17. Verfahren zur bestimmung der kolbenposition einer kolbenzylindereinheit und kolbenzylindereinheit. URL: <https://patents.google.com/patent/EP2759715A1>.
- Braun, S., Scheidt, M., Kipp, M., Leutenegger, P., 2017-04-05. Vorrichtung und verfahren zur positionsbestimmung eines zylinderskolbens. URL: <https://patentimages.storage.googleapis.com/cf/71/92/db2668332545b7/DE102015012799A1.pdf>.
- Breiman, L., 2001. Random Forests. *Machine Learning* 45, 5–32. doi:10/d8zjwq.
- Breiman, L., Friedman, J.H., Olshen, R.A., Stone, C.J., 1984. *Classification and Regression Trees*. Wadsworth and Brooks, Monterey, CA.
- Büchler, J., Fericean, S., Dorneich, A., Fritton, M., 2011-06-30. Verfahren und vorrichtung zur ermittlung der position eines kolbens eines kolbenzylinders mit mikrowellen. URL: <https://patents.google.com/patent/DE102009055445A1>.
- Chen, T., Guestrin, C., 2016a. XGBoost: A Scalable Tree Boosting System, in: *Proceedings of the 22nd ACM SIGKDD International Conference on Knowledge Discovery and Data Mining*, pp. 785–794. doi:10/gdp84q, arXiv:1603.02754.
- Chen, T., Guestrin, C., 2016b. Xgboost: A scalable tree boosting system. *CoRR abs/1603.02754*. URL: <http://arxiv.org/abs/1603.02754>, arXiv:1603.02754.
- Dorogush, A.V., Ershov, V., Gulin, A., 2018. CatBoost: Gradient boosting with categorical features support. arXiv:1810.11363.
- Fend, N., Audergon, L., Fritton, M., Dorneich, A., 2011-06-30. Verfahren zur bestimmung der position eines kolbens eines kolbenzylinders und mikrowellen-sensorvorrichtung. URL: <https://patents.google.com/patent/DE102009055363A1>.
- Frazier, B.W., Jr, T.M.A., Anlage, S.M., Ott, E., 2022. Deep-Learning Estimation of Complex Reverberant Wave Fields with a Programmable Metasurface , 30doi:10.1103/PhysRevApplied.17.024027.
- Glorot, X., Bengio, Y., 2010. Understanding the difficulty of training deep feedforward neural networks, in: *Proceedings of the Thirteenth International Conference on Artificial Intelligence and Statistics, JMLR Workshop and Conference Proceedings*. pp. 249–256.
- Glorot, X., Bordes, A., Bengio, Y., 2011. Deep Sparse Rectifier Neural Networks, in: *Proceedings of the Fourteenth International Conference on Artificial Intelligence and Statistics, JMLR Workshop and Conference Proceedings*. pp. 315–323.
- Goodfellow, I., Bengio, Y., Courville, A., 2016. *Deep Learning*. MIT Press. <http://www.deeplearningbook.org>.
- Gupta, S.H., 2020. Hand Movement Classification from Measured Scattering Parameters using Deep Convolutional Neural Network , 13doi:10.1016/j.measurement.2019.107258.
- He, K., Sun, J., 2014. Convolutional Neural Networks at Constrained Time Cost. arXiv:1412.1710.
- He, K., Zhang, X., Ren, S., Sun, J., 2015. Deep Residual Learning for Image Recognition. doi:10.48550/arXiv.1512.03385, arXiv:1512.03385.
- Hejazi, M.A., Gharehpetian, G.B., Moradi, G., Alehosseini, H.A., Mohammadi, M., 2011. Online monitoring of transformer winding axial displacement and its extent using scattering parameters and k-nearest neighbour method. *IET Gener. Transm. Distrib.* 5, 9. doi:10.1049/iet-gtd.2010.0802.
- Hien, P.T., Hong, I.P., 2021. Material Thickness Classification Using Scattering Parameters, Dielectric Constants, and Machine Learning. *Applied Sciences* 11, 10682. doi:10.3390/app112210682.
- Hirose, A., 2012. *Complex-Valued Neural Networks*. volume 400 of *Studies in Computational Intelligence*. Springer Berlin Heidelberg, Berlin, Heidelberg. doi:10.1007/978-3-642-27632-3.
- Hornik, K., Stinchcombe, M., White, H., 1989. Multilayer feedforward networks are universal approximators. *Neural Networks* 2, 359–366. doi:10/c4wch5.
- Husby, K., Myrvoll, T.A., Knudsen, O.Ø., 2019. Eddy Current duplex coating thickness Non-Destructive Evaluation augmented by VNA scattering parameter theory and Machine Learning , 6doi:10.1109/SAS.2019.8706003.
- Ioffe, S., Szegedy, C., 2015. Batch Normalization: Accelerating Deep Network Training by Reducing Internal Covariate Shift. doi:10.48550/arXiv.1502.03167, arXiv:1502.03167.
- Kang, Z., Catal, C., Tekinerdogan, B., 2020. Machine learning applications in production lines: A systematic literature review. *Computers & Industrial Engineering* 149, 106773. doi:10.1016/j.cie.2020.106773.
- Ke, G., Meng, Q., Finley, T., Wang, T., Chen, W., Ma, W., Ye, Q., Liu, T.Y., 2017. LightGBM: A Highly Efficient Gradient Boosting Decision Tree, in: *Advances in Neural Information Processing Systems*, Curran Associates, Inc.
- Kingma, D.P., Ba, J., 2017. Adam: A Method for Stochastic Optimization doi:10.48550/arxiv.1412.6980.
- Klambauer, G., Unterthiner, T., Mayr, A., Hochreiter, S., 2017. Self-Normalizing Neural Networks doi:10.48550/arxiv.1706.02515.
- LeCun, Y., Bengio, Y., Hinton, G., 2015. Deep learning. *Nature* 521, 436–444. doi:10/bmqp.
- LeCun, Y., Boser, B., Denker, J.S., Henderson, D., Howard, R.E., Hubbard, W., Jackel, L.D., 1989. Backpropagation Applied to Handwritten Zip Code Recognition. *Neural Computation* 1, 541–551. doi:10/bknd8g.
- Leutenegger, P., Zinner, T., Scheidt, D.M., Stucke, M., 2017-12-15. Hochdruckdurchführung zur durchführung eines koaxialkabels in einen hochdruckbereich. URL: <https://patents.google.com/patent/EP3349316A1>.
- Loshchilov, I., Hutter, F., 2017a. Decoupled weight decay regularization. arXiv preprint arXiv:1711.05101 doi:10.48550/arxiv.1711.05101, arXiv:1711.05101.

- Loshchilov, I., Hutter, F., 2017b. SGDR: Stochastic Gradient Descent with Warm Restarts. arXiv:1608.03983 [cs, math] doi:10/gp345z, arXiv:1608.03983.
- Ludwig, R., Brecht, P., 2000. RF Circuit Design: Theory and Applications. Prentice Hall.
- Maas, A.L., Hannun, A.Y., Ng, A.Y., 2013. Rectifier Nonlinearities Improve Neural Network Acoustic Models , 6.
- Mathès, M.W., Bromberg, Y., de Rosny, J., Popoff, S.M., 2021. Learning and avoiding disorder in multimode fibers. Phys. Rev. X 11, 021060. URL: <https://link.aps.org/doi/10.1103/PhysRevX.11.021060>, doi:10.1103/PhysRevX.11.021060.
- Morgan, D.E., 1994-06-28. Linear position sensor with means to eliminate spurious harmonic detections. URL: <https://patents.google.com/patent/US5325063A>.
- Nair, V., Hinton, G.E., 2010. Rectified Linear Units Improve Restricted Boltzmann Machines , 8.
- Narciso, D.A.C., Martins, F.G., 2020. Application of machine learning tools for energy efficiency in industry: A review. Energy Reports 6, 1181–1199. doi:10/gmcpk.
- Paszke, A., Gross, S., Massa, F., Lerer, A., Bradbury, J., Chanan, G., Killeen, T., Lin, Z., Gimelshein, N., Antiga, L., Desmaison, A., Kopf, A., Yang, E., DeVito, Z., Raison, M., Tejani, A., Chilamkurthy, S., Steiner, B., Fang, L., Bai, J., Chintala, S., 2019. Pytorch: An imperative style, high-performance deep learning library, in: Wallach, H., Larochelle, H., Beygelzimer, A., d'Alché-Buc, F., Fox, E., Garnett, R. (Eds.), Advances in Neural Information Processing Systems 32. Curran Associates, Inc., pp. 8024–8035. URL: <http://papers.neurips.cc/paper/9015-pytorch-an-imperative-style-high-performance-deep-learning-library.pdf>.
- Pedregosa, F., Varoquaux, G., Gramfort, A., Michel, V., Thirion, B., Grisel, O., Blondel, M., Prettenhofer, P., Weiss, R., Dubourg, V., et al., 2011. Scikit-learn: Machine learning in python. the Journal of machine Learning research 12, 2825–2830.
- Ramachandran, P., Zoph, B., Le, Q.V., 2017. Searching for Activation Functions. doi:10.48550/arXiv.1710.05941, arXiv:1710.05941.
- Rana, s., Dey, M., Tiberi, G., Vispa, A., Raspa, G., Duranti, M., Ghavami, M., Dudley, S., 2019. Machine Learning Approaches for Automated Lesion Detection in Microwave Breast Imaging Clinical Data , 12.
- Roshani, S., Jamshidi, M.B., Mohebi, F., Roshani, S., 2021. Design and Modeling of a Compact Power Divider with Squared Resonators Using Artificial Intelligence. Wireless Personal Communications 117, 2085–2096. doi:10.1007/s11277-020-07960-5.
- Rumelhart, D.E., Hinton, G.E., Williams, R.J., 1986. Learning representations by back-propagating errors. Nature 323, 533–536. doi:10/cvjdpk.
- Saroff, A.M., 2018. Complex Neural Networks for Audio , 115.
- Schonlau, M., Zou, R.Y., 2020. The random forest algorithm for statistical learning. The Stata Journal 20, 3–29. doi:10/ggqh2z.
- Simonyan, K., Zisserman, A., 2015. Very Deep Convolutional Networks for Large-Scale Image Recognition. arXiv:1409.1556.
- Srivastava, N., Hinton, G., Krizhevsky, A., Sutskever, I., Salakhutdinov, R., 2014. Dropout: A Simple Way to Prevent Neural Networks from Overfitting. Journal of Machine Learning Research 15, 1929–1958.
- Srivastava, R.K., Greff, K., Schmidhuber, J., 2015. Highway Networks. arXiv:1505.00387.
- Supriya, K., 2020. Trigger Word Recognition using LSTM. International Journal of Engineering Research and V9. doi:10/gp4prm.
- Trabelsi, C., Bilaniuk, O., Zhang, Y., Serdyuk, D., Subramanian, S., Joˆao, Mehri, S., Rostamzadeh, N., Bengio, Y., Christopher, 2018. Deep Complex Networks. arXiv pre-print server doi:10.48550/arxiv.1705.09792.
- Travassos, X.L., Avila, S.L., Ida, N., 2020. Artificial Neural Networks and Machine Learning techniques applied to Ground Penetrating Radar: A review. Applied Computing and Informatics 17, 296–308. doi:10.1016/j.aci.2018.10.001.
- Vaswani, A., Shazeer, N., Parmar, N., Uszkoreit, J., Jones, L., Gomez, A.N., Kaiser, Ł., Polosukhin, I., 2017. Attention is all you need. Advances in neural information processing systems 30. doi:10.48550/arxiv.1706.03762.
- Werbos, P., John, P., 1974. Beyond regression : New tools for prediction and analysis in the behavioral sciences / .
- White, J.F., 2004. High frequency techniques: An introduction to rf and microwave design and computer simulation. John Wiley & Sons.
- Yang, C.C., Bose, N., 2005. Landmine Detection and Classification With Complex-Valued Hybrid Neural Network Using Scattering Parameters Dataset. IEEE Transactions on Neural Networks 16, 743–753. doi:10.1109/TNN.2005.844906.
- Zeiler, M., Ranzato, M., Monga, R., Mao, M., Yang, K., Le, Q., Nguyen, P., Senior, A., Vanhoucke, V., Dean, J., Hinton, G., 2013. On rectified linear units for speech processing, in: 2013 IEEE International Conference on Acoustics, Speech and Signal Processing, IEEE, Vancouver, BC, Canada. pp. 3517–3521. doi:10.1109/ICASSP.2013.6638312.
- Zhang, Z., Wang, H., Xu, F., Jin, Y.Q., 2017. Complex-Valued Convolutional Neural Network and Its Application in Polarimetric SAR Image Classification. IEEE Transactions on Geoscience and Remote Sensing 55, 7177–7188. doi:10/gcqh44.